Available online at www.sciencedirect.com
ScienceDirect
Journal of Power Sources 160 (2006) 592–601
JOURNAL OF POWER SOURCES
www.elsevier.com/locate/jpowsour

Amorphous vanadium oxide films synthesised by ALCVD for lithium rechargeable batteries

K. Le Van [a], H. Groult [a,*], A. Mantoux [a], L. Perrigaud [a], F. Lantelme [a], R. Lindström [b], R. Badour-Hadjean [c], S. Zanna [b], D. Lincot [d]

[a] *Université Pierre & Marie Curie-Paris6, UMR 7612 CNRS, Laboratoire LI2C, Paris F-75005, France*
[b] *Laboratoire de Physico-Chimie des Surfaces (UMR CNRS 7045), ENSCP, 11 rue P.&M. Curie, 75231 Paris Cedex 05, France*
[c] *LADIR (UMR CNRS 7075), 2 rue Henri Dunant, 94320 Thiais, France*
[d] *LECA (UMR CNRS 7575), ENSCP, 11 rue P.&M. Curie 75231 Paris Cedex 05, France*

Received 15 March 2005; received in revised form 4 January 2006; accepted 13 January 2006
Available online 28 February 2006

Abstract

This study addresses the lithium insertion performances of amorphous vanadium oxide films, synthesized by atomic layer chemical vapour deposition (ALCVD). AFM and SEM investigations showed that the as-deposited films are amorphous, compact and homogeneous. As revealed by XPS and Raman spectroscopy, the ALCVD oxide films after deposition are mainly composed of V_2O_5, with V^{4+} surface content (about 10%). The insertion of Li^+ into the lattice was investigated in 1 M $LiClO_4$-PC. The results show that the electrochemical performances obtained with amorphous vanadium oxide films, with an optimal thickness of 200 nm (455 mAh g^{-1}, i.e. composition of $Li_{2.9}V_2O_5$), were superior to crystalline V_2O_5 films. The amorphous films exhibit higher capacity and better cycle ability even for deep lithium insertion ratio compared to crystalline V_2O_5 films. The chemical diffusion coefficients, deduced from numerical simulation of chronopotentiograms, were comprised between 3×10^{-12} and 10^{-13} cm^2 s^{-1} for a lithium insertion ratio comprised between 0 and 2.9. AFM and Raman spectroscopy performed before and after lithiation showed that neither the morphology nor the local order of the amorphous films were significantly affected by the insertion/extraction of lithium. Raman measurements also revealed that a very small amount of lithium are locally trapped in the oxide lattice.

Keywords: Amorphous vanadium oxide; Thin films; Atomic layer chemical vapour deposition; Lithium battery; AFM; Micro-Raman; XPS

1. Introduction

The reduction of the current and power requirements of electronic devices has promoted researches on the development of thin films electrodes for lithium microbatteries. Among the metal transition oxides potentially used as cathode materials, much attention has been paid to thin vanadium oxide (denoted VO) films. These oxide films exhibit good electrochemical performance versus the lithium insertion/deinsertion process, notably relatively high specific energy density [1–12]. Both amorphous and crystalline VO films can be used in lithium microbatteries. Nonetheless, in spite of their attractive properties, both crystallised and amorphous vanadium oxide films present some demerits. Crystalline V_2O_5 is characterised by the occurrence of phase transitions concomitant to the Li^+ insertion/deinsertion process, resulting in the formation of irreversible ω and γ phases at low potentials ($\leq$2.2 V versus Li/Li^+) [8,13,14]. The occurrence of these two lithiated phases reduces cycling performances of crystalline V_2O_5 in a wider potential region. To avoid these phase transitions, the potential window is usually limited to $\approx$3.8–2.9 V versus Li/Li^+ and as a consequence, the capacity is limited as well as the amount of lithium inserted into the host materials ($\leq$1 mole of Li per mole of V_2O_5). In addition, thermal annealing at temperature $\geq$500 °C in air of the as-deposited films is usually required to get well crystalline V_2O_5 and such a treatment leads to a high mechanical stress within the film that can affect the electrochemical performance of the films. In the case of amorphous VO [9,15–17], no phase transitions occur during the charge/discharge procedure. Therefore, the potential window can be extended, making

* Corresponding author. Tel.: +33 1 4427 3534; fax: +33 1 4427 3856.
E-mail address: groult@ccr.jussieu.fr (H. Groult).

0378-7753/$ – see front matter © 2006 Elsevier B.V. All rights reserved.
doi:10.1016/j.jpowsour.2006.01.049

possible increased capacity values and enhanced lithium retention into the host structure compared to crystalline VO. Thus, the higher tolerance to lithium insertion for amorphous VO compared to crystalline films make them attractive candidates for electrode application in lithium microbatteries. However, the amorphous films have often limitations for practical applications in thin-films batteries employing a liquid electrolyte due to undesirable reactions with the liquid electrolyte [9,15–18], which decrease the cycling performance. For example, Zhang et al. [9] have reported for amorphous VO films deposited by pulsed laser deposition, that the charge capacity drops more than 20% between the first and the second cycle due to the reduction of solvent on the electrode surface. Therefore, for ensuring long-term cycling efficiency and stability of amorphous VO in the presence of liquid electrolyte, one approach proposed in the literature is the protection of the amorphous VO thin film. For example, Lee et al. [16] recently proposed to coat the VO with an inorganic solid electrolyte, such as $LiAlF_4$. Another way is to develop new deposition techniques. Recently, thin VO films have been prepared by atomic layer chemical vapour deposition (ALCVD) from vanadyl triisopropoxide and water precursors [19–21]. This technique has several advantages compared to classical CVD. Among them, one can mention: (a) the strict control of the film thickness at atomic level [22,23] which allows to adjust the thickness of the microbattery (from several nanometers to several micrometers) depending on the required power; (b) the possibility to make gradual and/or alternate structures, i.e. to perform the deposition of all elements of the microbattery; (c) the use of very reactive precursors between them: consequently, the deposition can be done at low temperatures, that is very difficult with classical CVD since precursors are together present in the reaction chamber and (d) the possibility to form thin films deposited on plastic-based substrates or on substrates with a very large developed surface. Thus, the ALCVD technique can be considered as a new, very suitable and promising tool in the field of lithium microbattery.

Previously, the lithium intercalation performance in liquid electrolyte of ALCVD deposited annealed crystalline V_2O_5 has been investigated [21]. In that study a discrepancy of the cycling performances versus increasing film thickness (>200 nm) was shown. The objective of this work is to report for the first time the electrochemical performances of thin amorphous VO films prepared by ALCVD when they are used as cathode materials in lithium batteries in the presence of a liquid electrolyte. The expecting properties are: (1) good electrochemical performances (notably high discharge capacity); (2) high cycling efficiency (i.e. no capacity fading) and (3) high stability in the presence of liquid electrolyte (i.e. no degradation of the interface).

The first part of this paper is devoted to the structural and morphological characterisations of the VO films performed by SEM, AFM, micro-Raman and XPS. The second part is devoted to the electrochemical performance of the amorphous, as-deposited films versus lithium insertion/deinsertion reaction in organic solution, containing a lithium salt, deduced by chronopotentiometry.

2. Experimental section

2.1. Synthesis of vanadium films by ALCVD

The ALCVD apparatus is a commercial flow type F120 reactor (ASM-Microchemistry, Finland) using nitrogen (99.999% from Air Liquide, France) as carrier and purging gas; it is equipped with four plates reaction chamber, allowing to process a maximum of four 5 cm × 5 cm substrates. The ALCVD consisted in a sequential introduction of the reaction precursors, which allows to control the growth of the substrate at the atomic level. The deposition is achieved by repeating the following pulse sequence: t_1–t_4 up to the desired thickness, where "t_1–t_4" are the individual pulse times (in ms) of triisopropoxyvanadium oxide [$VO(OC_3H_7)_3$] (denoted VTOP henceforth provided by Alfa Aesar, USA), N_2, H_2O and N_2, respectively. Nitrogen gas was used as carrier and purging gas. The four pulses constitute one ALCVD cycle and the duration of one ALCVD cycle is 4 s. VTOP (vapor pressure of 0.29 Torr at 45 °C) reacts rapidly with water at room temperature and forms a vanadium oxide gel. The thin vanadium oxide films are obtained after evaporation of water at t_4.

The global reaction can be expressed as:

$$2VO(OC_3H_7)_3 + 3H_2O \rightarrow V_2O_5 + 6HOC_3H_7$$

Vanadium oxide thin films were deposited on titanium foils. Prior to deposition, titanium substrates were cleaned ultrasonically in dichloromethane, ethanol, rinsed in distilled water and dried under vacuum. VTOP was kept at 45 °C while the water source was kept at room temperature. The temperature in the reactor chamber was 105 °C. A linear variation of the thickness with the number of ALCVD cycles was observed [21]. Thus, Samples A and B obtained after 10,000 and 30,000 ALCVD cycles have a film thickness of 200 and 450 nm, respectively.

2.2. Film characterisations

2.2.1. Scanning electron microscopy

Scanning electron micrographies were obtained with a Jeol JEM 100 CX II transmission electron microscope equipped with a Jeol high resolution scanning attachment (STEM-SEM ASID 4D).

2.2.2. AFM analysis

Atomic force microscopy (AFM) investigations were performed both to observe the morphology and the roughness of the fresh vanadium oxide films and to study the effect of the insertion/deinsertion of Li^+ on the surface morphology. AFM imaging was performed using a Nanoscope III multimode scanning probe microscope (Digital Instruments) using a 100 μm × 100 μm piezoelectric scanner. The images were recorded under ambient conditions in contact mode using Si_3N_4 tips (Digital Instruments) with a spring constant of 0.58 N m^{-1}. Roughness factors were determined using the digital instruments image analysis software. Root mean square (R.M.S.) roughness , was determined from the AFM images collected before and

after insertion/extraction of Li^+: the analyses were performed at least on three replicas and for each one on eight different zones of 2.5 μm × 2.5 μm for ensuring reproducibility.

2.2.3. X-ray photoelectron spectroscopy

Surface analysis was performed by XPS. For these characterisations, V2p, O1s, and C1s core level spectra were recorded with a VG Escalab Mark II X-ray photoelectron spectrometer, with a Al Kα radiation ($h\nu = 1486.6$ eV), at a pass energy of 20 eV. The spectrometer was calibrated against the reference binding energies (BEs) of clean Ni and Au Samples (Ni $2p_{3/2}$ and Au $4f_{7/2}$ lines set at 852.8 and 84.0 eV, respectively). The take-off angles of the photoelectrons were 90°, with respect to the sample surface. In the XPS spectrometer, the base pressure of the analysis chamber was 3×10^{-10} Torr. To analyse the individual contributions of the $V2p_{3/2}$, O1s, and C1s core levels, peak decomposition was carried out with a commercial computer program (Eclipse provided by VG) using Gaussian/Lorentzian peak shapes, and a Shirley background. The O1s and $V2p_{3/2}$ regions were decomposed using a joint background. The C1s core level at 285.0 eV was used as an internal standard.

2.2.4. Micro-Raman spectrometry

The Raman spectra were recorded at room temperature using a micro-Raman system with a Dilor XY spectrometer equipped with a charge coupled device (CCD) detector. An argon ion laser (514.5 nm) was employed as the excitation source. A 50× objective was used to focus the laser light on sample surface to a spot of 5 μm^2 and the laser power was kept to 1 mW to avoid any degradation of the film. Finally, the spectra were measured in back-scattering geometry.

Results deduced with these techniques will be compared with those of crystallised V_2O_5, obtained after annealing of Samples A and B at 500 °C during 12 h in air. The annealed Samples are denoted Samples A500 and B500, respectively.

2.3. Electrochemical studies

The electrochemical performances of amorphous VO films versus the insertion/deinsertion of lithium cations into vanadium oxide films were investigated in 1 M $LiClO_4$-PC solution (provided by Merck and used as received) by chronopotentiometry. These experiments were carried out at room temperature in a glove box filled by argon ($C_{H_2O} \leq 5$ ppm) using coin cells. Both counter and reference electrodes were metallic lithium pellets. The galvanostatic charge–discharge curves and cyclic voltammograms were performed using a VMP Bio-Logic generator. Chronopotentiometry experiments were carried out at several constant current density between 4 and 1.5 V versus Li/Li^+. The charge and discharge capacity values were deduced from the analysis of the chronopotentiograms.

The diffusion coefficients of Li^+ into the V_2O_5 lattice were determined using an original theoretical approach described in detail elsewhere [24] which takes into account the influence of the variation of diffusion coefficient with concentration. This determination was performed by the fitting of chronopotentiograms.

3. Results and discussion

3.1. Physico-chemical analyses before lithiation

3.1.1. SEM observations

SEM investigations performed with Samples A and B are presented in Fig. 1 b and c, respectively (bar scale: 200 nm). For

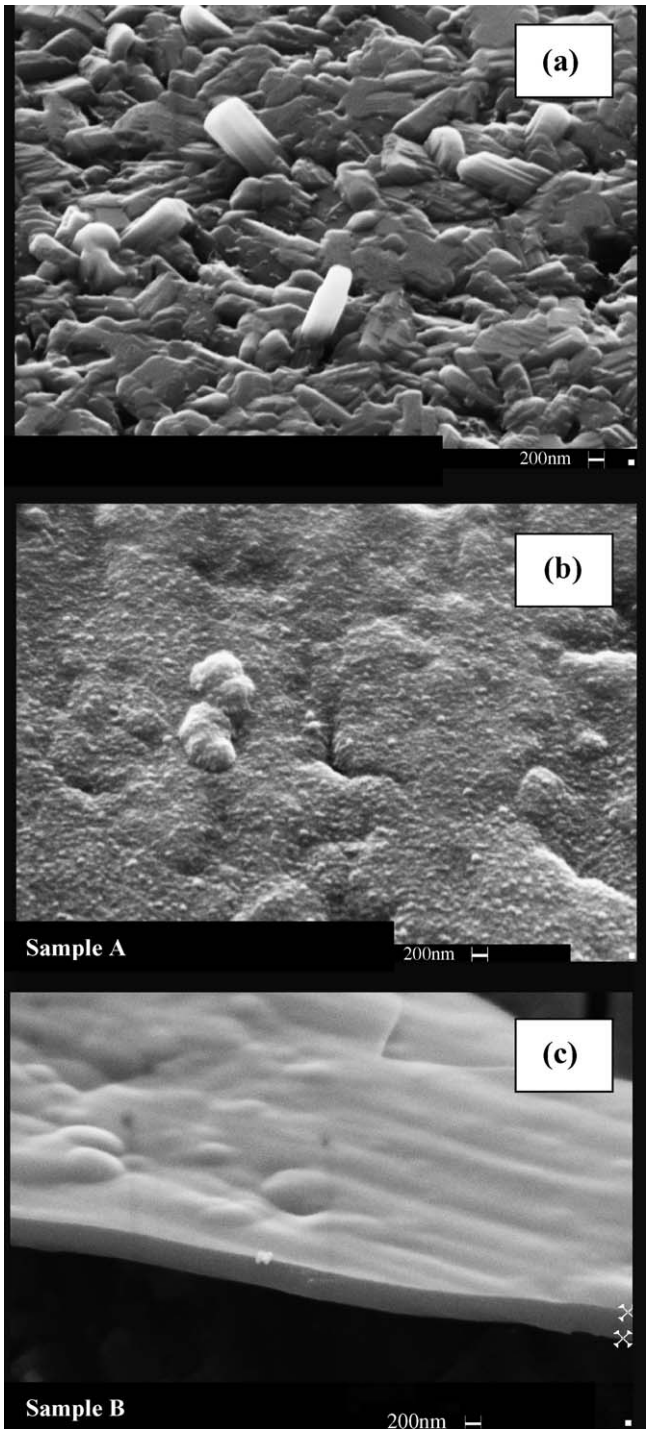

Fig. 1. : SEM images of (a) Sample B500 (Sample B heat-treated at 500 °C; thickness: 450 nm), (b) Sample A as-deposited; thickness: 200 nm), and (c) Sample B (as-deposited; thickness: 450 nm).

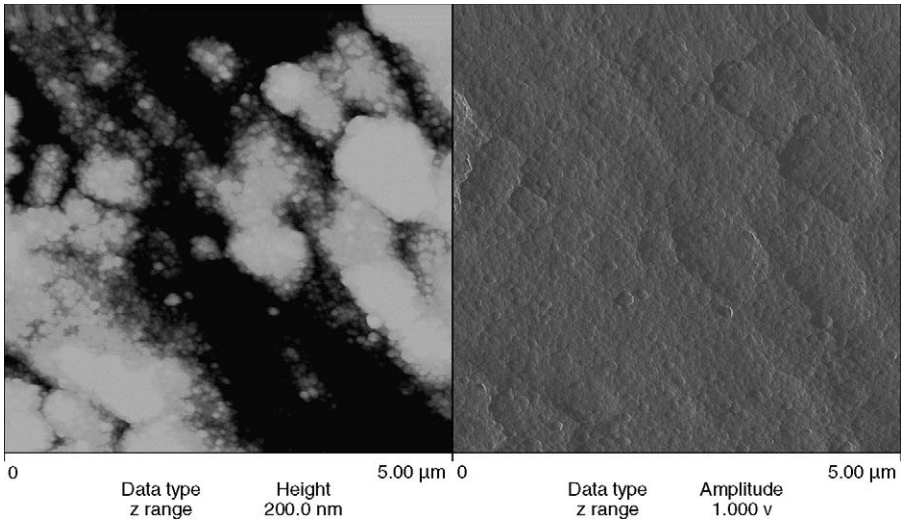

Fig. 2. AFM images (5 µm × 5 µm) of V_2O_5 as-deposited films by ALCVD on Ti substrate (Sample A; thickness: 200 nm).

comparison, images obtained with crystallised V_2O_5 (Sample B500) is also presented (Fig. 1a).

In the case of Sample B500 (Fig. 1a), the SEM image shows the presence of elongated plates with a rectangular form characteristic for crystalline V_2O_5. The images obtained for Samples A and B clearly differ from the crystalline sample. On the as-deposited films no evidence of V_2O_5 plates can bee seen, indicating that these films are amorphous. In addition, a strong influence of the film thickness on the morphology may be seen; the surface of the thicker Sample B film is more homogeneous and relatively smooth, whereas Sample A shows small globular shape particles of vanadium oxide. The cross-section image of Sample B (Fig. 1c) clearly evidences the high compactness and homogeneity of the film deposited by ALCVD. The conclusion that the as-deposited oxides are amorphous is supported by results from X-ray diffraction performed on Samples A and B that showed no diffraction lines.

3.1.2. AFM observation

Typical AFM images obtained with Sample A are presented in Fig. 2. The image clearly shows that the film is homogeneous and relatively smooth, characterized by small grains. The roughness (R.M.S.) value was found to be about 46 ± 2 nm (value determined on at least eight different areas of 6.25 µm^2). No significant difference in roughness was observed on the different replicas and different zones, indicating a good reproducibility in the AFM observation and in the sample preparation. The R.M.S. values obtained for Sample B is about two times lower, being 20 ± 2 nm. This variation is in good agreement with observations from SEM analysis, showing a higher smoothness of the VO films for Sample B.

3.1.3. Surface analyses by XPS

XPS measurements were performed to analyse the surface of the VO films. Sample A500 was used as reference sample for pure V_2O_5.

The survey spectra obtained for Samples A500, A and B are compared in Fig. 3a. All survey spectra display photoelectron peaks relative to V2s, V2p, V3s, V3p, C1s, O1s, and N1s and the characteristic Auger peaks, which result from a de-excitation process. In all spectra, the O1s line was found at 530.3 eV. The N1s photoelectron peak is due to the presence of residual nitrogen chemically adsorbed on the surface, resulting from N_2 used as carrier gas during the synthesis of the vanadium oxide films. The C1s photoelectron peak is due to contamination of the substrate by air. No difference was observed between the samples both for the position of the different photoelectron peaks (no chemical shift) and for the signal relative intensity, i.e. the composition of the surface is roughly the same, independently on film thickness.

For Samples A and B, the oxygen peak (Fig. 3b) for the freshly prepared ALCVD films is slightly broader than the reference; the shoulder at around 531.8 eV can be attributed to carbonate and corresponds well with the carbonate contribution of the C1s peak (not shown here). The carbonate contribution is slightly increased with increasing oxide thickness.

The $V2p_{3/2}$ core level was fitted to determine the nature and the oxidation state of vanadium present at the surface. For the reference Sample A500, the $V2p_{2/3}$ region is fitted with only one peak (Fig. Not shown here) located at 517.4 eV (FWHM = 1.56 eV) and assigned to V^{5+} as in V_2O_5. No peak for V^{4+} was detected for the annealed reference sample. However, the V2p regions for Sample A (Fig. 3c) can be decomposed in two peaks: one major peak analogous to V^{5+} (as in V_2O_5) at 517.4 eV and a minor at 516.1 eV, assigned to V^{4+}. The peaks are in accordance to reported XPS data for VO_2 and V_2O_5 [25–27]. From the integrals of the decomposition peaks, the relative contribution of V^{4+} is given to be about 10% for both Samples A and B, independently of thickness. The presence of V^{4+} in the amorphous films is in agreement with the green colour of the as-deposited films. Pure V_2O_5 films have a yellowish colour.

3.1.4. Micro-Raman spectrometry

Fig. 4a shows the Raman spectrum of Sample A500 used as reference. The well resolved spectrum exhibits several peaks at about 142, 194, 281, 299, 401, 476, 525, 698 and

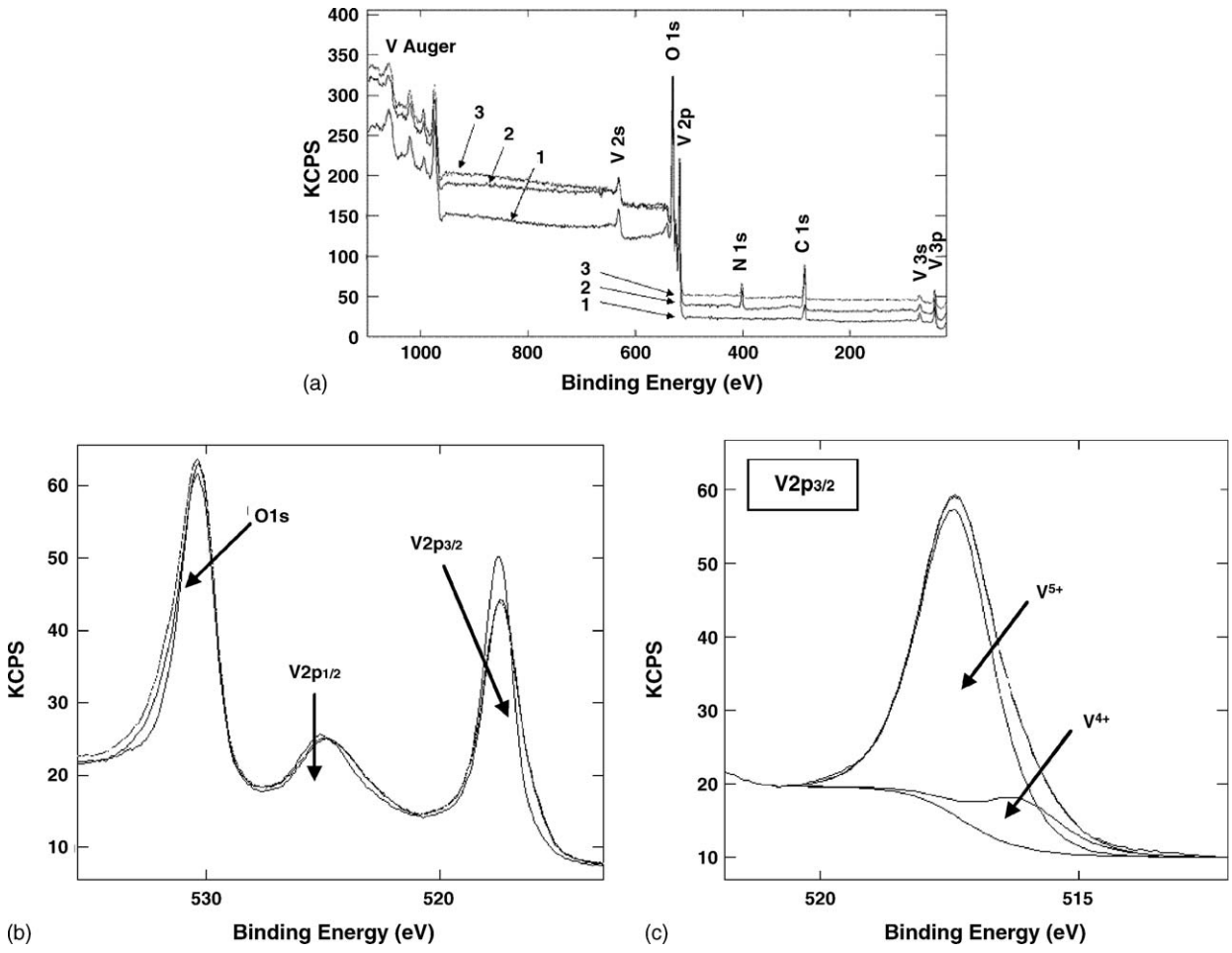

Fig. 3. XPS spectra: (a) *curve 1:* survey spectra of Sample A500 (Sample A heat-treated in air at 500 °C; thickness: 200 nm), *curve 2:* Sample A (as-deposited; thickness: 200 nm) and *curve 3*: Sample B (as-deposited; thickness: 450 nm); (b) O1s and V2p regions of Samples B500, A and B; (c) decomposition of $V2p_{2/3}$ region of Sample B.

992 cm^{-1} corresponding to the sequence observed for V_2O_5 single crystals [28] and polycrystalline films obtained by ALCVD [29]. The vibrational Raman active modes of V_2O_5 can be described in terms of vanadium–oxygen stretching modes, vanadium–oxygen–vanadium bending vibrations and translational modes. The peak centered at 992 cm^{-1} is assigned to the stretching mode related to the shortest vanadium oxygen bond V = O. The prominent peak at 142 cm^{-1} is attributed to the skeleton bent vibration. It has been related to a deformation of the bond between different molecular units in the plane of the layers. Its presence provides evidence for the long-range order of Sample A500.

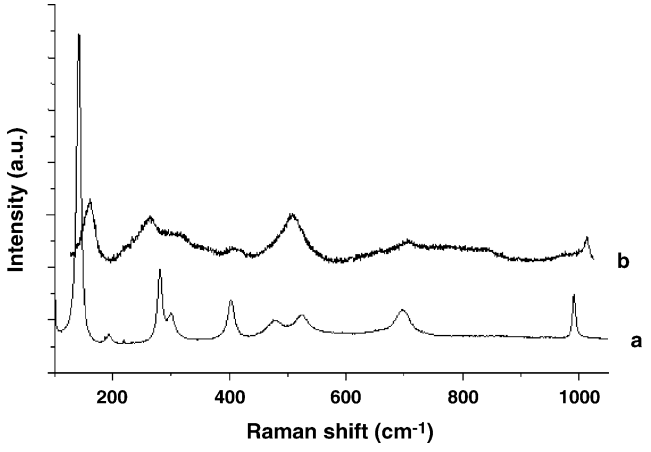

Fig. 4. Raman spectra of (a) Sample A500 (Sample A heat-treated at 500 °C; thickness: 200 nm); (b) Sample A (as-deposited; thickness: 200 nm).

The Raman spectrum of Sample A (Fig. 4b) shows a strong reduction of the intensity, a general broadening of the Raman bands and several frequency shifts compared to the polycrystalline A500 reference sample. The broad band at 507 cm^{-1} can be decomposed into two components located at 493 and 516 cm^{-1} which probably trace their origin back to the two peaks at 476 and 525 cm^{-1} in polycrystalline V_2O_5. The complex band structure in the 200–350 cm^{-1} region can be decomposed into three components at 240, 264 and 309 cm^{-1} which are probably related to the peaks observed at 281 and 299 cm^{-1} in polycrystalline V_2O_5. The strongest peak at 142 cm^{-1} in polycrystalline V_2O_5, appears in sample A with a strongly reduced intensity and a frequency value shifted towards higher wavenumbers, 160 cm^{-1}. Furthermore, the half-width of this rigid layer-like mode increases from 6 cm^{-1} in polycrystalline V_2O_5 to 14 cm^{-1} the Sample A, suggesting some random potential fluctuations

arising form the amorphous state. On the other hand, the sharper band at 1014 cm^{-1} in Sample A compared to 992 cm^{-1} in the reference sample might indicate a strengthened V=O bond in the distorted VO_5 pyramid (by eventual breaking of one equatorial V–O bond) or can also be assigned to an IR-active mode visible in the Raman spectra of disordered vanadium oxide phases [30].

All these observations are in agreement with the partial loss of the long range order, the occurrence of structural disorder and a disordered distribution of the bond lengths in Sample A.

3.2. Electrochemical studies

3.2.1. Charge/discharge cycling

Fig. 5 shows the first five charge–discharge cycles (rate: *C*/10) between 1.5 and 4.0 V versus Li/Li^+ for Sample A. The initial open circuit voltage of the amorphous V_2O_5 film is about 3.33 V versus Li/Li^+. This value is slightly lower than that usually observed for crystalline V_2O_5, due to the presence of small amount of V^{4+}. No plateau is observed during charge and discharge procedures indicating the absence of phase transitions concomitant to the Li^+ insertion/deinsertion process as usually evidenced for crystalline orthorhombic V_2O_5 films. The absence of plateaus is characteristic for amorphous films. In the present potential range the insertion/deinsertion reaction is reversible. Similar results were obtained with Sample B. Notice that at the end of the delithiation process, the green initial colour of the film (due to the presence of V^{4+}) turns to a yellow colour, characteristic of V_2O_5. It indicates that V^{4+} is re-oxidised in V^{5+} during the process.

The capacity values, deduced at the end of the delithiation process, as well as the fading capacity during cycle life were examined from the analysis of the chronopotentiograms. Fig. 6 gives the evolution of the capacity for Samples A and B. The best electrochemical performance was obtained for Sample A, with the lowest thickness (200 nm). For this sample, the capacity slightly decreases during the first cycles before reaching a constant value of about 455 mAh g^{-1} (≈155 μAh (μm × cm^2)$^{-1}$) at *C*/10, giving rise to a composition of about $Li_{2.9}V_2O_5$. This value is much larger than that reported for crystalline ALCVD V_2O_5 films with the same film thickness (200 nm). Mantoux [21] recently reported on values of 125 mAh g^{-1} (45 μAh (μm × cm^2)$^{-1}$) and 220 mAh g^{-1} (80 μAh (μm × cm^2)$^{-1}$) between 3.8–2.8 V versus Li/Li^+ and 3.8–2.2 V versus Li/Li^+, respectively. With increasing thickness,

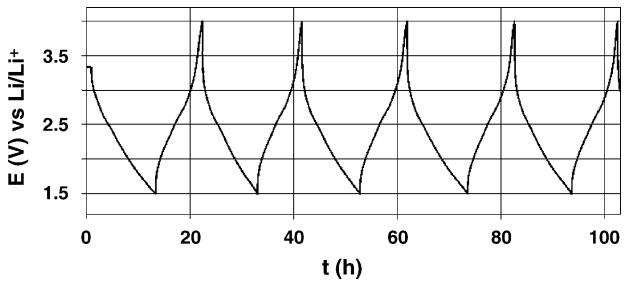

Fig. 5. Five first charge–discharge chronopotentiograms obtained with Sample A in 1 M $LiClO_4$-PC at room temperature. Potential window for the charge–discharge cycling: 4.0–1.5 V vs. Li/Li^+. Rate: *C*/10. $S = 0.785\ cm^2$.

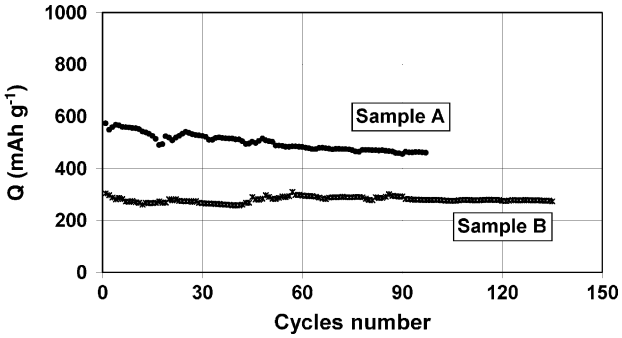

Fig. 6. Evolution of the reversible capacity obtained in 1 M $LiClO_4$-PC with Samples A and B. Potential window for the charge–discharge cycling: 4.0–1.5 V vs. Li/Li^+. Rate: *C*/10. $S = 0.785\ cm^2$.

the capacity values decrease, probably due to the fact that the insertion/deinsertion process only occurs into the outer oxide layer of a finite thickness and not in the entire bulk. Thus, the reversible capacity of Sample B (450 nm) is only about 275 mAh g^{-1} after 100 cycles. For crystallised ALCVD V_2O_5 thin films with the same thickness, a drastic decrease of the capacity was observed only after few cycles [21]. This was explained by a decrease of the cohesion between the crystallites within the film and/or adhesion to the substrate surface, as a result of annealing. Without thermal annealing, the cohesion of the film is significantly enhanced, and so, the electrochemical performance. For comparison, the capacity of Sample B is constant upon cycling (Fig. 6), indicating a good stability of the film upon insertion/extraction of lithium. Moreover, in contrast to amorphous VO films deposited by other techniques such as PLD [9], the use of liquid electrolyte does not give rise to capacity fading upon cycling.

Finally, the influence of the charge–discharge rate (from *C*/10 to 25 °C) on the insertion/deinsertion process was studied. The results obtained with Samples A and B are presented in Fig. 7. As shown, the capacity recorded is large, even for very high discharge rates. For example, Sample A exhibits a capacity of about 140 mAh g^{-1} at 25 °C (i.e. ≈50 μAh (μm × cm^2)$^{-1}$). In addition, in spite of very high charge/discharge rates, the reversibility of the insertion/deinsertion reaction is good, as illustrated in Fig. 8 showing the 10 first cycles for Samples A and B at 25 °C.

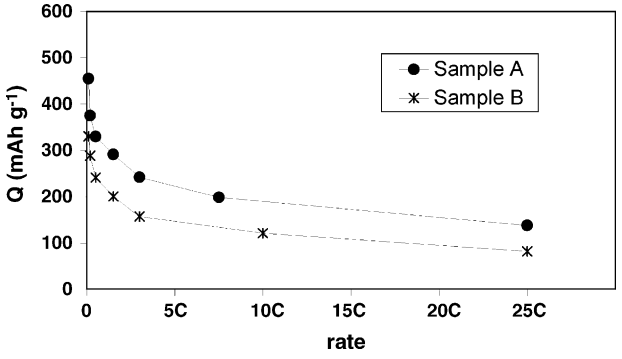

Fig. 7. Influence of charge/discharge rate on the reversible capacity obtained in 1M $LiClO_4$-PC with Samples A and B. Potential window for the charge–discharge cycling: 4.0–1.5 V vs. Li/Li^+. $S = 0.785\ cm^2$.

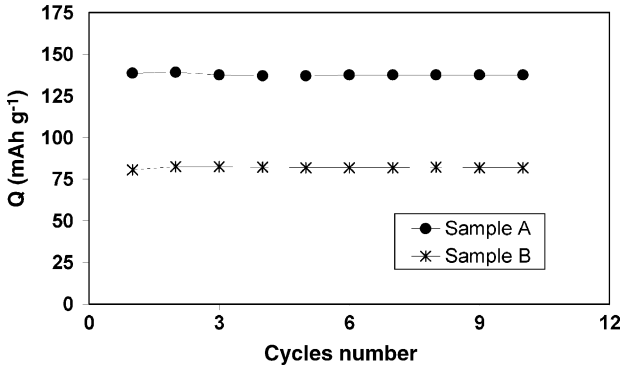

Fig. 8. Evolution of the reversible capacity obtained in 1 M $LiClO_4$-PC with Samples A and B during the 10 first cycles. Potential window: 4.0–1.5 V vs. Li/Li^+. Rate: 25C. $S = 0.785\,cm^2$.

3.2.2. Determination of the kinetics parameters

The insertion/deinsertion process is governed by the diffusion of Li^+ into the host structure and this phenomenon must be both reversible and rapid for good battery performance. The determination of the kinetics parameters, notably the lithium diffusion coefficients can be carried out using an original approach described in detail elsewhere [24]. It is based on fitting of the chronopotentiogram curves, taking into account the dependence of the lithium diffusion coefficient on concentration. By this, chronopotentiometry may provide information on the intercalation/deintercalation process over a larger concentration range. The values obtained from the fit of the chronopotentiograms are usually different from those obtained from the impedance measurements. This is simply explained by the fact that the diffusion coefficient values, deduced from impedance measurements, are obtained at equilibrium and correspond to a known stoichiometric composition and cell voltage. In contrast, the new approach proposed here provides more accurate determination of the transport mechanism and more correct of values for the diffusion coefficient.

The determination of the diffusion coefficient may briefly be explained as follows: if one consider a classical reversible redox reaction, the flux of electroactive species, for a one-dimensional system, is defined as:

$$J = \frac{nF}{RT} Dc \nabla E = \frac{nF}{RT} Dc \frac{dE}{dx} \tag{1}$$

In a non-stationary situation, the concentration obeys the following mass balance equation:

$$\frac{dc}{dt} = -\nabla J = -\frac{nF}{RT} \frac{d}{dx} \left(Dc \frac{dE}{dc} \frac{dc}{dx} \right) \tag{2}$$

In solid state, the non-dependence of the diffusion coefficient on the composition of the diffusing medium is not usually observed. For example, in the case of lithium intercalation into host materials a dependence of the lithium coefficient diffusion is often pointed out and therefore, must be considered in the calculation to obtain a correct description of experimental results. Therefore, for a reliable description of the reality, a variation of $D = f(c)$ for the derivation of the term in the right side of Eq. (1) must be taken into account. The diffusion equation including the factors of solid state-diffusion is now:

$$\frac{dc}{dt} = -\frac{nF}{RT} \left\{ Dc \frac{dE}{dc} \frac{d^2c}{dx^2} + \left[\left(D + c \frac{dD}{dc} \right) \frac{dE}{dc} + Dc \frac{d^2E}{dc^2} \right] \left(\frac{dc}{dx} \right)^2 \right\} \tag{3}$$

The potential of the electrochemical intercalation of Li^+ into the host materials during the reduction step is defined by:

$$E = E^0 - \frac{RT}{nF} \ln(\gamma c) \tag{4}$$

and so, Eq. (3) can be written:

$$\frac{dc}{dt} = D \left(1 + c \frac{d(\ln \gamma)}{dc} \right) \frac{d^2c}{dx^2} + \left\{ \frac{dD}{dc} \left(1 + c \frac{d(\ln \gamma)}{dc} \right) + D \left(\frac{d(\ln \gamma)}{dc} + c \frac{d^2(\ln \gamma)}{dc^2} \right) \right\} \left(\frac{dc}{dx} \right)^2 \tag{5}$$

The integration of diffusion Eq. (5) is rather impossible. Therefore, digital simulation is the only way to treat the problem comprehensively. For that, one considers that the space (x coordinate) is divided into small intervals of length Δx and the time into small time steps, Δt [31]. In the finite difference scheme the continuous functions are finitized, with centred finite difference for the space derivatives:

$$\left(\frac{d^2c}{dx^2} \right)_t = \frac{c^t_{x-\Delta x} - 2c^t_x + c^t_{x+\Delta x}}{(\Delta x)^2} \tag{6}$$

$$\left(\frac{dc}{dx} \right)^2_t = \frac{(c^t_{x+\Delta x} - c^t_x)(c^t_x - c^t_{x-\Delta x})}{(\Delta x)^2} \tag{7}$$

$$\left(\frac{dc}{dt} \right)_x = \frac{c^{t+\Delta t}_x - c^t_x}{\Delta t} \tag{8}$$

The calculation follows a forward explicit scheme in which the composition profile of diffusing species at time $t + \Delta t$ is computed from the profile at time t according to Eq. (5), with

$$c^{t+\Delta t}_x = c^t_x + \left(\frac{\Delta t}{(\Delta x)^2} \right) \left\{ D \Gamma_a (c^t_{x-\Delta x} - 2c^t_x + c^t_{x+\Delta x}) + \left(\Gamma_a \frac{dD}{dc} + D \Gamma'_a \right) (c^t_{x+\Delta x} - c^t_x)(c^t_x - c^t_{x-\Delta x}) \right\} \tag{9}$$

Γ_a is thermodynamic factor and Γ'_a its derivative,

$$\Gamma_a = 1 + c^t_x \frac{d \ln \gamma}{dc} \tag{10}$$

$$\Gamma'_a = \frac{d \ln \gamma}{dc} + c^t_x \frac{d^2 \ln \gamma}{dc^2} \tag{11}$$

The function, $\ln(\gamma)$, is deduced from the titration curve. The function, $D = f(c)$, is assumed to be known. The current density, j_0, is calculated from the flux of electroactive species at the electrode surface.

The first step of this method is to record the evolution of the open circuit voltage (OCV) and closed circuit voltage

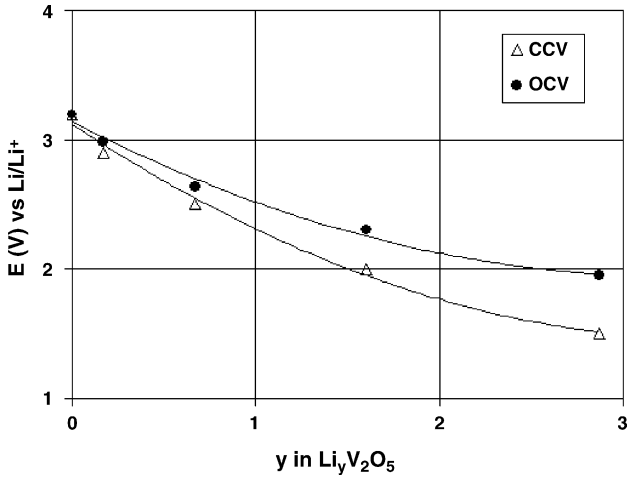

Fig. 9. △: Closed circuit voltage (CCV) and ●: equilibrium open circuit voltage (OCV) of Sample A in PC-$LiClO_4$ 1 M at 25 °C vs. lithium intercalation ratio, y in $Li_yV_2O_5$. Rate: *C*/10.

(CCV). At first, a constant current is applied to the working electrode (amorphous V_2O_5) during a sufficient time, t_1, in order to reach a constant discharge potential denoted CCV_1 (called closed circuit voltage), which corresponds to a discharge ratio, y_1, and a composition of $Li_{y1}V_2O_5$. Secondly, the current is cut and the system relaxes towards an equilibrium state, corresponding to an equilibrium potential OCV_1 (open circuit voltage). The latter is considered to be reached when the derivation of potential is less than 0.2 mV h^{-1}. The procedure is repeated until a CCV value of 1.5 V versus Li/Li^+ is reached.

The evolution of the OCV and CCV curves for Sample A is presented in Fig. 9. As shown previously, the discharge potential gradually decreases and the recharge potential gradually increases, without any plateau versus lithium intercalation ratio, y. This indicates that the amorphous oxide is a single ternary phase electrode material $Li_yV_2O_5$ with a continuous variation of its composition on discharge and recharge. As illustrated in Fig. 10, the calculated curve fits very well the experimental curve in considering a diffusion process with a variable diffusion coefficient. Moreover, no significant discrepancy appears between the two curves. The detailed analysis of the diffusion mechanism involves the thermodynamic enhancement of the diffusion transport, which is directly deduced from the emf measurement. Therefore, this treatment of the electrochemical experiments is more coherent.

According to the value of the thermodynamic factor calculated from the OCV curve, the calculated chemical diffusion coefficient is given by:

$$\tilde{D} = -D\frac{\mathrm{d}\ln a}{\mathrm{d}\ln c} = D\left(1 + c\frac{\mathrm{d}(\ln\gamma)}{\mathrm{d}c}\right) \quad (12)$$

The variation of the $\tilde{D}_{Li}$ values for Samples A and B deduced from the fitting of the chronopotentiograms using the theoretical approach described above are presented in Fig. 11. Whatever the sample, a gradual decrease of $\tilde{D}_{Li}$ is observed due to the decreasing probability to find an unoccupied site close to an

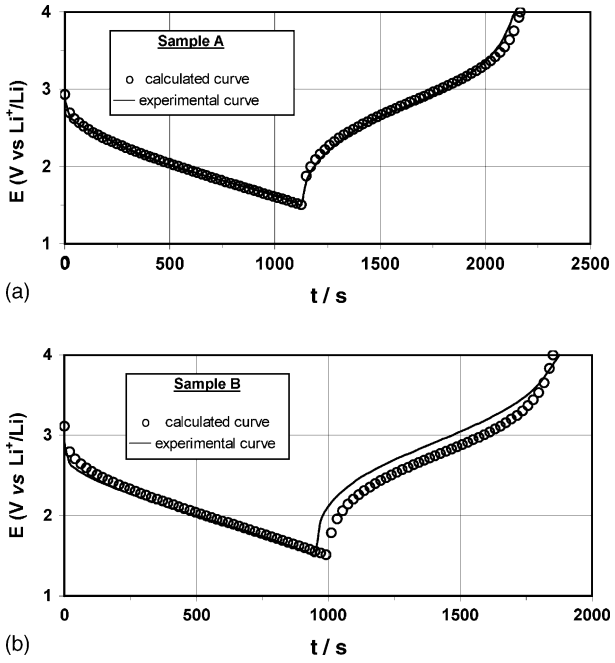

Fig. 10. Experimental and calculated chronopotentiograms for lithium insertion in amorphous thin V_2O_5 films in PC-$LiClO_4$ 1 M at 25 °C. (a) Sample A; (b) Sample B. Rate: *C*/10. S = 0.785 cm^2.

occupied one. The highest $\tilde{D}_{Li}$ values are obtained with Sample A which exhibits the best electrochemical performances upon cycling, i.e. the highest capacity values. For this sample, $\tilde{D}_{Li}$ varies from 3×10^{-12} to 1.2×10^{-13} $cm^2\ s^{-1}$ for increasing y-values comprised between 0 and 3.

3.3. Physico-chemical analyses after lithiation

Finally, Samples A and B were also studied after several charge/discharge cycles both by AFM and micro-Raman spectrometry to study the effect of the insertion/deinsertion of Li^+ on the nature and the roughness of the vanadium oxide films. Each analyse was performed in a de-lithiated state, i.e. after reoxidation of the sample.

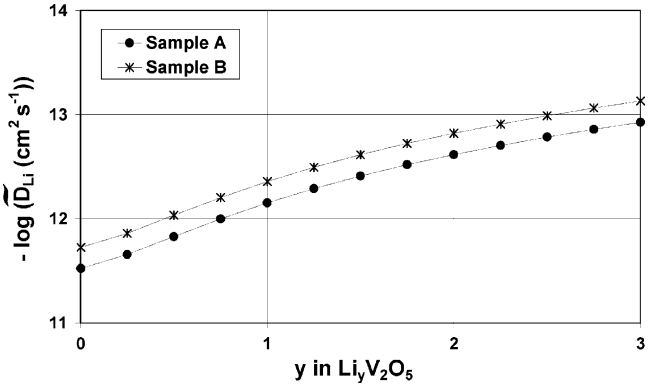

Fig. 11. Values of the chemical diffusion coefficient, $\tilde{D}_{Li}$ obtained from the fitting of chronopotentiograms with Samples A and B in PC-$LiClO_4$ 1 M at 25 °C vs. lithium insertion ratio, y in $Li_yV_2O_5$. Rate: *C*/10. *S* = 0.785 cm^2.

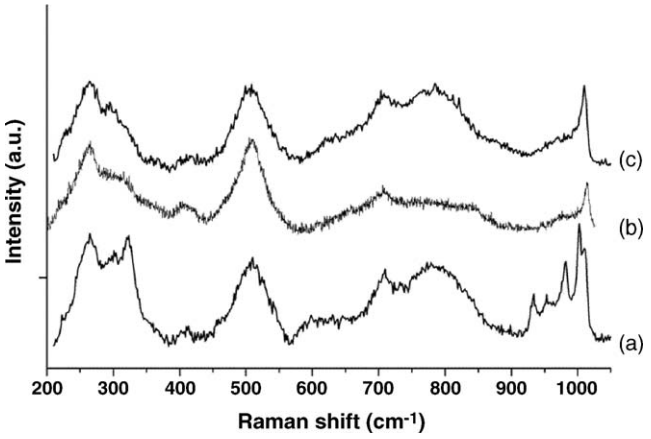

Fig. 12. Raman spectra of (a) and (c) Sample A after 20 charge–discharge cycles (*C*/10) between 4.0 and 1.5 V vs. Li/Li^+ in PC-$LiClO_4$ 1 M; (b) Sample A before cycling.

3.3.1. AFM observations after lithiation

No modification of the film morphology after cycling was observed by AFM (not shown here). In accordance, no significant difference in roughness was observed on the different replicas and different zones. For example, the R.M.S. value obtained for Sample A was determined to 43 ± 2 nm, which is very similar to the value obtained for the same sample before cycling (46 ± 2 nm), indicating good stability of the vanadium film upon cycling.

3.3.2. Micro-Raman spectroscopy after lithiation

Raman spectra were recorded at different points of the surface (at least 10). In the major part of the surface, the Raman spectra of the cycled Sample A (Fig. 12c) are very similar to that of the starting amorphous material (Fig. 12b). Nevertheless, in the minor part of the surface, some new features in the high frequency region hint that the Li insertion may have caused some irreversible changes onto the vanadyl V=O bond (Fig. 12a). Besides the Raman peak at 1010 cm^{-1}, characteristic for the starting material, new Raman bands were observed at lower frequencies, namely at 1002, 981, 956 and 933 cm^{-1}. The shift towards lower frequency may indicate a weakening of the vanadyl bond upon lithium insertion and is in good agreement with the results previously obtained on polycrystalline V_2O_5 films [29]. The persistence of such peaks in the cycled sample can be interpreted by some remaining lithium ions trapped in the oxide lattice after reoxidation. Again, one must notice that this observation was done only in some parts of the surface.

4. Conclusion

We report here for the first time the electrochemical properties of amorphous vanadium oxide films deposited by atomic layer chemical vapour deposition (ALCVD). Micro-Raman and XPS analyses revealed that these films are constituted mainly of V_2O_5 but, according to the XPS measurements, small amount (≈10%) of V^{4+} is present in the amorphous films, at least on the film surface, independently on film thickness.

In contrast to annealed vanadium oxides films, the insertion/deinsertion reaction may be performed in a very large potential window, between 4 and 1.5 V versus Li/Li^+, without any modification of the electrochemical performance. The best electrochemical performance was obtained for the amorphous film with a thickness of 200 nm. For this film, the reversible capacity, reached between 4.0 and 1.5 V versus Li/Li^+, was close to 455 mAh g^{-1} (≈155 μAh (μm × cm^2)$^{-1}$) after about 100 cycles. The capacity of the amorphous films is much higher than that obtained for the annealed films. For comparison, the capacity was only 220 mAh g^{-1} (80 μAh (μm × cm^2)$^{-1}$), obtained between 3.8 and 2.2 V versus Li/Li^+, for the crystalline film with the same film thickness. In addition, no capacity fading was observed with amorphous films, independently on thickness, as was observed with crystallised vanadium oxide films thicker than 200 nm. Finally, the yellowish colour of the film observed after cycling is an indication that the V^{4+} initially present is oxidised into V^{5+}.

The results presented in this paper demonstrate the very good lithium intercalation properties of the amorphous vanadium oxides films deposited by ALCVD. In contrast to annealed crystalline films and also amorphous films obtained by other deposition techniques, the amorphous films prepared by ALCVD can support stress generated by insertion/deinsertion of lithium into the host structure without significant structural damages and degradation upon cycling, even at low potentials. Therefore, as-deposited vanadium oxide films prepared by ALCVD technique are attractive new materials for lithium intercalation applications and can be considered as promising candidates for cathode materials in lithium microbatteries. Finally, this work is the first step for the preparation of a complete all-solid state thin film microbattery.

Acknowledgements

The authors are grateful to Dr. J.-P. Pereira-Ramos for fruitful discussions, Dr. S. Borensztajn for the SEM imaging, Dr. S. Durand-Vidal for his helpful assistance for AFM observations, and Mr. P. Genevois for his technical assistance in making the electrochemical cells used in this study.

References

[1] J.-M. Cocciantelli, M. Menetrier, C. Delmas, J.P. Dourmec, M. Pouchard, M. Broussely, J. Labat, Solid States Ionics 78 (1995) 143.
[2] B. Scrosati, in: C.A. Vincent, B. Scrosati (Eds.), Modern batteries, 2nd ed., Arnold, London, 1997, p. 199 (Chapter 7).
[3] M. Wakihara, Mat. Sci. Eng. R: reports 33 (2001) 109.
[4] J.-P. Pereira-Ramos, N. Baffier, G. Pistoia, in: G. Pistoia (Ed.), Lithium batteries: new materials developments and perpectives, Elsevier, Amsterdam, 1994, p. 281.
[5] M.S. Whittingham, Prog. Solid State Chem. 12 (1978) 41.
[6] C. Julien, S. Radhakrishna (Eds.), Trends in materials science, Narosa Publishing House, London, 1996, p. 24.
[7] E. Potiron, A. Le Gal La Salle, A. Verbaere, Y. Piffard, D. Guyomard, Electrochim. Acta 45 (1999) 197.
[8] D. Gourier, A. Tranchant, N. Baffier, R. Messina, Electrochim. Acta 37 (1992) 2755.

[9] J.-G. Zhang, J.M. McGraw, J. Turner, D. Ginley, J. Electrochem. Soc. 144 (1997) 1630.
[10] D.W. Murphy, P.A. Christian, Science 205 (1979) 651.
[11] J.B. Bates, G.R. Gruzalski, N.J. Dudney, C.F. Luck, X.H. Yu, S.D. Jones, Solid State Technol. 36 (1993) 59.
[12] A. Mantoux, H. Groult, E. Balnois, P. Doppelt, L. Gueroudji, J. Electrochem. Soc. 150 (2004) A368.
[13] J.-M. Cocciantelli, J.P. Doumerc, M. Pouchard, M. Broussely, J. Labat, J. Power Sources 34 (1991) 103.
[14] C. Delmas, H. Cognac-Auradou, J.-M. Cocciantelli, M. Ménetrier, J.P. Doumerc, Solid State Ionics 69 (1994) 257.
[15] C. Sanchez, J. Livage, J.P. Audiere, A. Madi, J. Non-Cryst. Solids 65 (1984) 285.
[16] S.-H. Lee, H.M. Cheong, P. Liu, C.E. Tracy, Electrochem. Sol. Lett. 6 (2003) A102.
[17] S. Passerini, W.H. Smyrl, M. Berrettoni, R. Tossici, J.M. Rosolen, R. Marassi, F. Decker, Solid Stat Ionics 90 (1996) 5.
[18] J.B. Bates, N.J. Dudney, D.C. Lubben, G.R. Gruzalski, B.S. Kwak, X. Yu, R.A. Zuhr, J. Power Sources 54 (1995) 58.
[19] J.-C. Badot, S. Ribes, E.B. Yousfi, V. Vivier, J.-P. Pereira-Ramos, N. Baffier, D. Lincot, Electrochem. Solid-State Lett. 3 (2000) 485.
[20] A. Mantoux, J.-C. Badot, N. Baffier, J. Farcy, J.-P. Pereira-Ramos, D. Lincot, H. Groult, J. Phys. IV France 12 (2002) Pr2–P111.
[21] A. Mantoux, Thesis, Paris (2003).
[22] T. Suntola, M. Simpson, Atomic layer epitaxy, Chapman and Hall, New York, 1990.
[23] T. Suntola, D.T.J. Hurle (Eds.), Handbook of crystal growth, vol. 3, Elsevier, Amsterdam, 1994, p. 601 (Part B, Chapter 14).
[24] F. Lantelme, A. Mantoux, H. Groult, D. Lincot, J. Electrochem. Soc. 150 (2003) A1202.
[25] J. Mendialdua, R. Casanova, Y. Barbaux, J. Electron. Spectrosc. Relat. Phenom. 71 (1995) 249.
[26] A.M. Salvi, F. Decker, F. Varsano, G. Speranza, Surf. Interface Anal. 31 (2001) 255.
[27] Z.M. Zhang, V.E. Henrich, Surf. Sci. 321 (1994) 133.
[28] L. Abello, E. Husson, Y. Repelin, G. Lucazeau, Spectrochim. Acta 39A (1983) 641.
[29] R. Baddour-Hadjean, V. Golabkan, J.P. Pereira-Ramos, A. Mantoux, D. Lincot, J. Raman Spectrosc. 33 (2002) 631.
[30] L. Abello, E. Husson, Y. Repelin, G. Lucazeau, J. Solid State Chem. 56 (1985) 379.
[31] F. Lantelme, Y. Zongsen, X. Zeqiang, X. Xishan (Eds), Modelling and simulation in fused salts electrowinning of metals, in modelling and simulation in metallurgical engineering and material science, Metallurgical Industry Press, Beijing, 1996, pp. 133–139.